Large magnetodielectric coupling in layered perovskite Eu_2TiO_4

Yang Zhang,[1] Yudai Hasegawa,[1] Shingo Kitano,[1] Lihong Liu,[3] Tohru S. Suzuki,[3] Wei Yi,[1] Hirofumi Akamatsu,[2] and Koji Fujita[1*]

[1]*Department of Material Chemistry, Graduate School of Engineering, Kyoto University, Katsura Nishikyo-ku, Kyoto 615-8510, Japan*
[2]*Department of Applied Chemistry, School of Engineering, Kyushu University, Motooka, Fukuoka 812-0053, Japan*
[3]*Optical Ceramics Group, Research Center for Electronic and Optical Materials, National Institute for Materials Science, Tsukuba, Ibaraki, 305-0047 Japan*

Perovskite-type $EuTiO_3$, which is quantum paraelectric and G-type antiferromagnetic (AFM) in the bulk form, has attracted great attention due to its strong spin-lattice coupling and strain-induced multiferroic in thin film form. In this study, significant magnetodielectric (MD) coupling is demonstrated in K_2NiF_4-type ferromagnetic (FM) layered perovskite Eu_2TiO_4, which features alternating rock-salt (Rs)-type EuO layers and perovskite (Pv)-type $EuTiO_3$ layers. We find a dielectric anomaly as a local minimum of permittivity near the ferromagnetic transition temperature (T_C = 9.5 K) in the temperature-dependent permittivity under zero magnetic field. Remarkably, an applied magnetic field induces a substantial increase in permittivity at T_C (approximately 22% at 3 T), which is three times larger than that observed in bulk $EuTiO_3$. Our experimental and first-principles studies reveal that the insertion of EuO layers in Eu_2TiO_4 enhances the Eu-f/Ti-d orbitals hybridization through pseudo-strain in the $EuTiO_3$ layers, as well as modifies the magnetic exchange paths that favor ferromagnetism over antiferromagnetism. The enhanced hybridization highlights the role in the large MD coupling played by AFM superexchange interactions via the Ti 3d state, which competes with indirect FM interactions via the Eu 5d state. Our findings demonstrate the potential of layered structure to control MD coupling, paving the way for new strategies in designing MD materials.

I. INTRODUCTION

The coupling between static electrical and magnetic properties is an interesting effect from the perspective of both fundamental physics and potential applications [1]. This coupling is exemplified by multiferroic materials where two or more primary ferroic orders — such as ferroelectrics, (anti)ferromagnetics, and ferroelastics — coexist. The interaction between these order parameters leads to many interesting effects [2–4]. Moreover, the growing interest in novel dielectric devices has spurred the exploration of the magnetodielectric (MD) coupling, wherein the dielectric properties are tunable by application of magnetic field [5]. This effect has been observed in various materials including Gd_2CuO_4, [6] $YMnO_3$, [7] $EuTiO_3$, [8] $BiMnO_3$ [9] Pb_2MnO_4 [10], and $TbMnO_3$ [55].

Among materials exhibiting MD coupling, perovskite oxides $EuMO_3$ (M = Ti, Zr, Hf) containing Eu^{2+} with $4f^7$ spins (S = 7/2) have attracted significant attention due to their manipulable magnetic properties and strong spin-lattice coupling [11–14]. For example, bulk $EuTiO_3$ exhibits a G-type antiferromagnetic (AFM) ordering below the Néel temperature (T_N = 5.3 K) [15,16], quantum paraelectric (PE) behavior, and a 7% change in permittivity at 2 K under a magnetic field of 1.5 T [8]. Subsequent theoretical and experimental studies have demonstrated switchable ground states between AFM-PE and ferromagnetic-ferroelectric (FM-FE) phases through strain engineering in epitaxial $EuTiO_3$ films. For instance, FM behavior can be induced by the one-dimensional (1D) out-of-plane elongation, while the FM-FE phase arises from 2D biaxial tension (e.g., due to a $DyScO_3$ substrate) or from three-dimensional (3D) tension caused by negative pressure (e.g., due to the embedded MgO cylinders) [17–21]. Additionally, recent studies on bulk $(Eu,A)ZrO_3$ solid solutions (A = Ca, Sr, Ba) have demonstrated that the 3D lattice expansion generated by chemical substitution at the A-site can alter magnetic properties, inducing a transition from AFM to FM states [22].

Regarding the AFM-to-FM switching behavior of $EuMO_3$, Akamatsu *et al.* reported comprehensive computational studies, revealing the key role played by the hybridization between the Eu 4f orbitals and M *n*d orbitals. In $EuTiO_3$, the G-type AFM state consists of antiparallel spin alignments between the two-interpenetrating face-centered cubic (FCC) sublattices of Eu ions. The magnetic interactions are primarily governed by nearest-neighbor (NN) AFM interactions ($J_1 < 0$) and the next-nearest-neighbor (NNN) FM interactions ($J_2 > 0$). The transition from AFM to FM ordering is linked to changes in lattice structure, such as 1D lattice expansion, 2D biaxial strain, or 3D strain-induced negative pressure as mentioned above. These

*fujita.koji.5w@kyoto-u.ac.jp

structural changes modify the balance between FM indirect exchange through Eu 5d states (Eu-Eu) and AFM superexchange via Ti 3d states (Eu-Ti-Eu), which leads to a reversal in the sign of J_1 from negative to positive that is favored by the FM state.

The hybridization of Eu-4f/Ti-3d states is also considered the dominant source of MD effects in $EuTiO_3$. The microscopic origin of MD effects has been discussed both theoretically and experimentally in terms of the spin-phonon coupling [23,24]. The soft phonon mode, which involves the vibration of Ti^{4+} ions against the O^{2-} octahedra, contributes the most to permittivity and thus dominates MD coupling. The spin alignments of Eu^{2+} ions can significantly impact permittivity through the Eu-Ti-Eu superexchange interactions [25]. In $EuTiO_3$ thin films with 3D tensile strain, the MD coupling (~0.1% at 1.5 T) has been observed with a 3% lattice expansion [19], and the magnitude of the coupling is approximately 70 times weaker than that in bulk $EuTiO_3$ (~7% at 1.5 T). This reduction can be attributed to the volume expansion, which weakens the Eu-Ti-Eu interactions and suppresses the MD coupling. The strong dependence of spin-phonon coupling on the energy levels of empty d states of B-site cations explains why strong spin-lattice coupling has not been observed in other related perovskite oxides, such as $EuZrO_3$ (~0.3% at 5 T) [14,25,26].

Eu_2TiO_4, a Ruddlesden-Popper (RP) perovskite oxide, (space group $I4/mmm$), features alternately stacked monolayers of perovskite (Pv) $EuTiO_3$ and rock-salt (RS) EuO, as shown in Fig. 1. The insertion of the RS layers introduces additional exchange bridges between Eu^{2+} ions, enhancing the hybridization between Eu 4f and 5d orbitals. This facilitates indirect FM exchange interactions between neighboring Eu^{2+} ions [15]. The Pv units in Eu_2TiO_4, separated by RS layers, form a tetragonal unit cell. Compared to cubic $EuTiO_3$ in bulk form (lattice parameter $a = b = c = 3.905$ Å), the Pv units in Eu_2TiO_4 are compressed by approximately 0.5% and 6.5% in the in-plane and out-of-plane directions, respectively. This compression can be interpreted as a pseudo-uniaxial strain resulting from the intrinsic chemical nature of the layered perovskite structure. Such pseudo strain is expected to enhance the overlap of Eu 4f and Ti 3d orbitals in the Pv layers and thus to strengthen the spin-lattice coupling. In this respect, we focus on the potential MD effect in Eu_2TiO_4.

In this study, we demonstrate substantial MD coupling (~22% at 3T) near T_C in the layered perovskite Eu_2TiO_4. A combined study of structure analysis and first-principles calculations suggest that the enhanced Eu-4f/Ti-3d orbital hybridization in the Pv layers may be the origin of the large MD coupling. This strong spin-lattice coupling arises from the interplay between RS and Pv layers, allowing for the coexistence of FM interactions and strong MD coupling—a combination that is not achievable in the simple perovskite oxide $EuTiO_3$. The layered structure plays a unique role in integrating the magnetic and dielectric properties within this system.

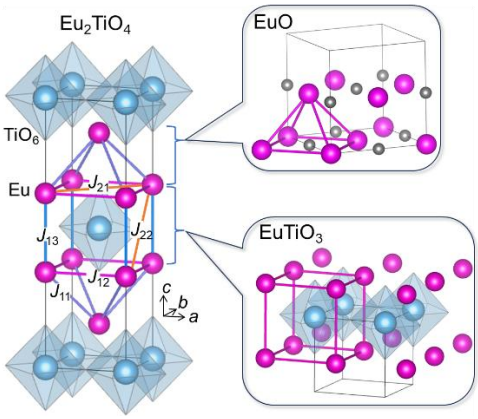

FIG. 1. Crystal structure of Eu_2TiO_4 with RS-type EuO and Pv-type $EuTiO_3$ layers. The NN interactions J_{1m} (m = 1, 2, 3) and NNN interactions J_{2n} (n = 1, 2) are shown with different color lines.

II. METHOD

The polycrystalline samples of Eu_2TiO_4 were prepared by the solid-state reaction method. Reagent-grade Eu_2O_3 and TiO_2 (both 99.9% pure, sourced from Kojundo Chemical Laboratory Co, Ltd) were used as starting materials. Prior to use, Eu_2O_3 was preheated at 900°C for 12 h to remove water and carbon dioxide. The solid-state synthesis was carried out in two steps. First, EuO precursors were prepared by the reduction of Eu_2O_3 using graphite carbon (C): Eu_2O_3 and C were mixed at a mole ratio of 1:1.2, pelletized, and heated at 1400°C under flowing of Ar gas for 6 h. Next, EuO and TiO_2 were mixed, pelletized, and heated at 1350°C under flowing Ar gas for 6 h to get Eu_2TiO_4. We also prepared high-density ceramic samples (> 98% density) by spark plasma sintering (SPS). First, Eu_2TiO_4 powder was loosely placed into a graphite die with a diameter of 10 mm. Then, the SPS treatment was carried out in a vacuum condition at a heating rate of 100°C/min under a uniaxial pressure of 90 MPa using a SPS machine (SPS1050, Fuji Electronic Industrial Co., Ltd, Japan). Finally, the sintering was conducted at 1450°C with a dwelling time of 1 min.

The phase purity of the final products, including SPS specimens, was checked by x-ray diffraction (XRD) using Smart-Lab diffractometer (Rigaku) with

Cu Kα radiation. (λ = 1.5418 Å). High-resolution synchrotron x-ray diffraction (SXRD) was performed at room temperature using the large Debye−Scherrer cameras with MYTHEN solid-state detectors installed at the beamlines BL02B2 (SPring-8). The incident beam was monochromatized to λ = 0.774702 Å. Finely ground powder samples were sieved through a 32μm mesh sieve and put into a Pyrex capillary with 0.1 mm inner diameter. The sealed capillary was rotated during measurements to reduce the effect of preferential orientation. The SXRD data collected were analyzed by the Rietveld method [27] using a Jana program [28].

Magnetization measurements were carried out with a superconducting quantum interference device (SQUID) magnetometer (MPMS, Quantum Design). Temperature dependence of magnetic susceptibilities was measured in a range 2–300 K at an external magnetic field of 0.01 T. The field dependence of magnetization was recorded at 2 and 9.5 K in magnetic fields up to 5 T.

Dielectric properties were measured with an LCR meter (Agilent E4980) in the temperature range 2–300 K in the magnetic field of 0–5 T utilizing a home-made dielectric measurements probe coupled with the physical property measurement system (PPMS, Quantum Design). 50 nm/20 nm Au/Ti electrodes were deposited on the top and bottom surface of an Eu_2TiO_4 pallet (6 mm diameter) using electron beam evaporation (HITACHI, Japan).

First-principles density functional theory (DFT) calculations were carried out for Eu_2TiO_4 (space group: $I4/mmm$) and $EuTiO_3$ (space group: $Pm\bar{3}m$) using the projector augmented-wave (PAW) method [29,30] as implemented in the VASP code [31–36]. To reduce the computational costs, the generalized gradient approximation-PBEsol (GGA-PBEsol) [37–39] and HSE06 hybrid functional [40–42] were used for structural optimizations and electronic structure calculations, respectively. The PAW datasets with radial cutoffs of 1.5, 1.3, and 0.8 Å were used with a plane-wave cutoff energy of 550 eV. The following states were described as valence electrons: $4f^7$, $5s^2$, $5p^6$, $6s^2$ for Eu; $3d^2$, $4s^2$ for Ti; and $2s^2$, $2p^4$ for O. FM spin configurations were considered for Eu_2TiO_4 and $EuTiO_3$. The lattice constants and internal coordinates were optimized until the residual stress and forces converged to 0.2 GPa and 1 meV/Å, respectively. A phonon band structure was calculated for Eu_2TiO_4 using the PHONOPY code [43]. The crystal orbital Hamilton population (COHP) between Eu and Ti atoms was calculated using the LOBSTER code [44,45]. The VESTA code was used to visualize crystal structures [46].

III. RESULTS

According to laboratory XRD data, the main phase of the synthesized products was identified as Eu_2TiO_4 with an n = 1 RP (K_2NiF_4)-type structure. The ^{151}Eu Mössbauer spectrum shows that almost all the europium ions exist as Eu^{2+} (see Fig. S1 and Table S1 in the Supplemental Material (SM) [51]). Figure 2 shows the SXRD pattern at room temperature. The main reflections can be indexed by a tetragonal unit cell with lattice parameters of $a = b$ = 3.88619(1) Å, and c = 12.54039(4) Å. The observed reflection conditions indicate the tetragonal symmetry (space group $I4/mmm$), in agreement with previous observation on Eu_2TiO_4 [15]. A negligibly small amount of EuO impurities (less than 1 wt%) is detected. Rietveld refinement with the $I4/mmm$ structure model converges to a good reliability index R_{wp} (weighted profile R factor) of 6.65%. Separate occupancy refinement reveals no deviation from the ideal composition. Detailed structural parameters obtained from the refinement are summarized in Table S2 in SM [51].

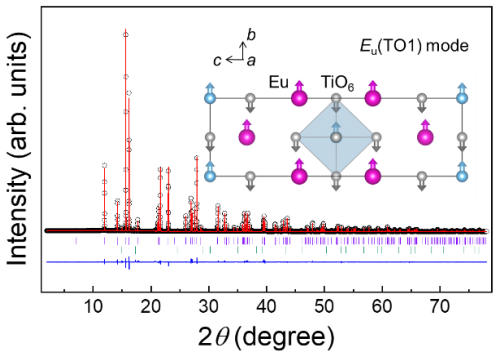

FIG. 2. SXRD pattern (λ = 0.774702 Å) of n = 1 RP-type Eu_2TiO_4 at 300 K and fitting curve obtained by Rietveld refinement with the $I4/mmm$ structure model. Black circles and red solid curves represent the observed and the calculated intensities, respectively. The blue solid line at the bottom indicates the difference between the experimental and calculated patterns. Purple and green ticks show the peak positions of Eu_2TiO_4 and EuO, respectively. The inset shows a schematic diagram for the movement of atoms in the E_u(TO1) mode in Eu_2TiO_4.

The crystal structure of n = 1 RP-type Eu_2TiO_4 can be interpreted as alternating layers of TiO_2 and EuO planes stacked along the c-axis, as illustrated in Fig. 1. The stacking sequence follows a TiO_2-EuO-EuO pattern, with the second EuO layer being shifted by 1/2a along the [110] direction relative to the first EuO layer. From the structural refinement, the $EuTiO_3$ unit in the Pv layer shows lattice parameters of a_{Pv} = b_{Pv} = 3.88619(1) Å, c_{Pv} = 3.65819(1) Å, indicating a compressed c-axis compared to its in-plane dimensions.

Before presenting the dielectric properties and MD coupling of Eu_2TiO_4, it is crucial to first examine the magnetic characteristic of our Eu_2TiO_4 samples. Temperature dependence of magnetic susceptibility (χ–T) exhibits an FM transition around T_C = 9.5 K [see Fig. 3(a)]. A Curie-Weiss analysis in the temperature range 15 K ≤ T ≤ 300 K yields effective magnetic moment μ_{eff} = 7.84(1)μ_B, consistent with the expected 7.8 μ_B for Eu^{2+} ions in a $4f^7$ ($J = S = 7/2$) configuration. The analysis also reveals a Weiss temperature θ_W = 10.05(2) K, indicating that FM interactions are dominant. These values of μ_{eff} and θ_W are in good agreement with those reported previously for polycrystalline Eu_2TiO_4 samples [47].

Temperature-dependent dielectric permittivity $\varepsilon(T)$ under zero magnetic field at 1 MHz is displayed in Fig. 3(b). Below 30 K, we observed a negligible dependence of permittivity on frequency between 1 kHz and 1 MHz, along with a relatively low dielectric loss ($\tan\delta$ < 0.3). The permittivity decreases with decreasing the temperature, indicating that Eu_2TiO_4 behaves distinctly from quantum paraelectric $EuTiO_3$. As the temperature further decreases, a local minimum of permittivity is observed near 9.5 K, corresponding to the T_C. This anomaly of permittivity is smeared out when the magnetic field of 5 T is applied, suggesting the presence of MD coupling in this system.

The magnetic field dependence of magnetization (M–H) and permittivity (ε–H) at 2 and 9.5 K is comparatively shown in Figs. 3(c) and 3(d), respectively. At 2 K [see Fig. 3(c)], the magnetization increases with the magnetic field increasing and reaches its saturation around 1.2 T. The saturation magnetization is 6.7 μ_B/Eu^{2+}, which is close to the full moment of free Eu^{2+} (7 μ_B/Eu^{2+}). Meanwhile, the permittivity is independent of the magnetic field and slightly decreases beyond 1.2 T. The slight decrease in the permittivity under high fields can be attributed to magnetostriction [54], similar to what was observed in the strain-induced FM $EuTiO_3$ thin films [19]. The field-independent permittivity at low magnetic fields could result from the cancellation of positive contribution from magnetic structure changes and negative contribution from magnetostriction (see Fig. S5).

Remarkably, at T = 9.5 K [see Fig. 3(d)], both magnetization and permittivity increase simultaneously when the magnetic field is applied up to 3 T. This is indicative of significant MD coupling, and the permittivity enhancement is about 22% at 3 T, which is three times larger than that observed in $EuTiO_3$ (7% at 1.5 T) [8]. Note that the resistivity in our samples exceeds 10^6 Ω·cm below 30 K. In addition, a high frequency (1 MHz) was employed for the dielectric measurements in this study to mitigate the influence of charge carriers. Therefore, the contribution from the magnetoresistance could be negligible.

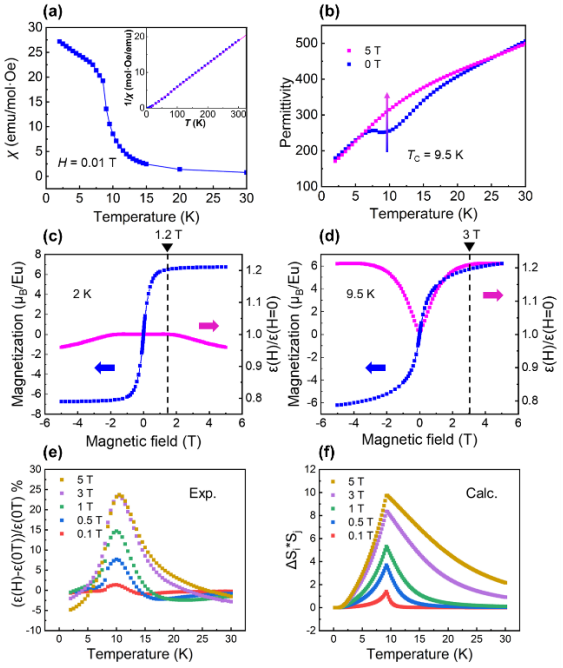

FIG. 3. (a) Temperature dependence of magnetic susceptibility χ (=M/H) of Eu_2TiO_4 collected at 0.01 T. The inset shows the inverse susceptibility $1/\chi$ with Curie-Weiss fitting (pink line). (b) The permittivity of Eu_2TiO_4 as a function of temperature (2 K ≤ T ≤ 30 K) measured at 0 and 5 T under a frequency of 1 MHz. (c) and (d) Variation of magnetization and $\varepsilon(H)/\varepsilon(H=0)$ of Eu_2TiO_4 with magnetic field at (c) 2 K and (d) 9.5 K. (e) and (f) Temperature dependence of (e) $[\varepsilon(H)-\varepsilon(H=0)]$ / $\varepsilon(H=0)$ % and (f) $\Delta\langle \boldsymbol{S}_i\cdot\boldsymbol{S}_j\rangle$ obtained by subtracting $\langle \boldsymbol{S}_i\cdot\boldsymbol{S}_j\rangle$ data at 0 T from those at 0.1, 0.5, 1, 3, and 5 T.

In bulk $EuTiO_3$, permittivity as a function of temperature and magnetic field can be represented using the following equation [8]:

$$\varepsilon(T,H) = \varepsilon(T,0)\,(1 + \alpha < \boldsymbol{S}_i \cdot \boldsymbol{S}_j >) \ , \quad (1)$$

where $\varepsilon(T, 0)$ is the permittivity at zero magnetic field. $\langle \boldsymbol{S}_i\cdot\boldsymbol{S}_j\rangle$ is the spin pair correlation between nearest-neighboring Eu^{2+}, and α is the coupling constant between spin correlation and permittivity [8]. To estimate $\langle \boldsymbol{S}_i\cdot\boldsymbol{S}_j\rangle$ in Eu_2TiO_4, molecular-field calculations were conducted based on a Heisenberg model under an assumption that the 4f spins of Eu^{2+} (S = 7/2) are located on a tetragonal lattice with FM ordering. The Heisenberg Hamiltonian of the spin system is given by:

$$H^{me} = \sum_{ij} J_{ij} \cdot \boldsymbol{S}_i \cdot \boldsymbol{S}_j \ , \quad (2)$$

where J_{ij} represents the exchange constants between spins $\boldsymbol{S}_i$ and $\boldsymbol{S}_j$, with a restriction on considering only the NN and NNN interactions. This approach helps us evaluate the magnetic exchange interactions and their impact on the dielectric properties of Eu_2TiO_4. We used the exchange interaction parameters obtained with the previous first-principles calculations [48] (see Fig. 1, and Fig. S2, and Table S3 in the SM [51]): J_{11}/k_B = 0.2 K, J_{12}/k_B = 0.08 K and J_{13}/k_B = 0.0 K for NN interactions, J_{21}/k_B = 0.08 K and J_{22}/k_B = 0.04 K for NNN interactions, where k_B is the Boltzmann constant. In the molecular-field calculation, $<\boldsymbol{S}_i\cdot\boldsymbol{S}_j>$ is obtained as the product of $<\boldsymbol{S}>$ on two sublattices. To further analyze the impact of a magnetic field on the dielectric properties, we calculated the change in spin pair correlation:

$$\Delta\langle \boldsymbol{S}_i \cdot \boldsymbol{S}_j \rangle = \langle \boldsymbol{S}_i \cdot \boldsymbol{S}_j \rangle_H - \langle \boldsymbol{S}_i \cdot \boldsymbol{S}_j \rangle_0 \ , \quad (3)$$

where $<\boldsymbol{S}_i\cdot\boldsymbol{S}_j>_H$ and $<\boldsymbol{S}_i\cdot\boldsymbol{S}_j>_0$ are the spin pair correlations under finite and zero magnetic field, respectively. Figure 3(e) illustrates the relative permittivity change:

$$\frac{[\varepsilon(H)-\varepsilon(0)]}{\varepsilon(0)} \times 100\% \ , \quad (4)$$

in comparison with $\Delta<\boldsymbol{S}_i\cdot\boldsymbol{S}_j>$ [Fig. 3(f)]. The calculated results show remarkable agreement with the experimental findings, indicating that the MD effect in Eu_2TiO_4 is primarily governed by the pair correlation of the Eu^{2+} spins. The magnetodielectric coupling constant is $\alpha = 2.4 \times 10^{-2}$, which obtained by Eq. (1) for Eu_2TiO_4, is the largest among perovskite-type oxides with Eu^{2+} occupying the A-sites, e.g., $EuZrO_3$ ($\alpha = 1.1 \times 10^{-4}$) [14] and $EuTiO_3$ ($\alpha = 2.74 \times 10^{-3}$) [8], highlighting the unique magnetodielectric properties of Eu_2TiO_4.

IV. DISCUSSION

A. Magnetic properties of Eu_2TiO_4

We start with a brief survey of the magnetic properties of Eu_2TiO_4. For perovskite and related oxides with Eu^{2+} occupying the A-sites, both AFM and FM interactions coexist between the nearest-neighboring (NN) Eu^{2+}–Eu^{2+} pairs. Hence, the magnetism of these oxides alters depending on the relative strength of the competing magnetic interactions, i.e., the sign of J_1. In bulk $EuTiO_3$, Eu^{2+} ions have six nearest neighbors within the cubic lattice, where the indirect FM exchange via the Eu 5d states and the AFM superexchange via the Ti 3d states coexist. The G-type AFM state of bulk $EuTiO_3$ appears due to the AFM superexchange via the Ti 3d states. Moreover, it was also suggested that the third nearest neighbor magnetic exchange (J_3) may play a crucial role in the MD coupling in $EuTiO_3$ [49]. In the case of J_3, the exchange occurs between Eu ions at opposite corners of a cube through the central Ti ion, forming a 180° Eu-Ti-Eu superexchange pathway, further highlighting the significance of Eu-Ti-Eu superexchange interactions.

In contrast, the layered structure in Eu_2TiO_4 introduces significant changes in the magnetic exchange paths: the number of NN Eu^{2+}–Eu^{2+} pairs increases from 6 in $EuTiO_3$ to 9 in Eu_2TiO_4. Specifically, the insertion of an RS layers between the Pv units introduces four additional Eu^{2+}-Eu^{2+} pairs along the <11√2> direction (exchange constant J_{11}), maintaining four Eu^{2+}-Eu^{2+} interactions along the <100> and <010> directions (exchange constant J_{12}), while it eliminates one of two Eu^{2+}-Eu^{2+} pairs along the <001> direction (exchange constant J_{13} for the remaining pair); (see Table. S3 in the SM [51]). The absence of Ti atoms in the RS-type EuO layers results in the exclusive presence of FM indirect exchange (positive J_{11}). Namely, the additional magnetic exchange pathways in Eu_2TiO_4 leads to the FM ground state.

Previous first-principles studies of Eu_2TiO_4 have suggested competition between FM and AFM exchanges within the Pv layers (near zero J_{13}) and in the RS-Pv interlayers (slightly positive J_{12}) [48]. To compare such competition in Eu_2TiO_4 with those in $EuTiO_3$, we checked the refined structure data: in Eu_2TiO_4, the Pv layers, sandwiched by the RS layers, have a tetragonal unit cell ($a_{Pv} = b_{Pv}$ = 3.88619(1) Å, c_{Pv} = 3.65819(1) Å), which is compressed by approximately 0.5% and 6.5% in the in-plane and out-of-plane directions, respectively, relative to the cubic unit cell of bulk $EuTiO_3$ (lattice parameter $a = b = c$ = 3.905 Å). This uniaxial compression effectively reduces the Eu-Ti distance in Eu_2TiO_4 (3.301 Å) compared to that in bulk $EuTiO_3$ (3.382 Å). This pseudo-strain along the c-axis caused by the insertion of the RS layers works to enhance the overlap between Eu 4f and Ti 3d orbitals in the Pv layers, potentially strengthening the spin-lattice coupling.

B. Magnetodielectric effect of Eu_2TiO_4

The observation of large MD coupling constant in the Eu_2TiO_4 raises two questions: What is the origin of MD coupling in FM Eu_2TiO_4? Additionally, why is the magnitude of MD coupling even larger than bulk $EuTiO_3$?

According to Lyddane-Sachs-Teller (LST) relation, the permittivity is connected to the optical phonon frequency:

$$\frac{\varepsilon_0}{\varepsilon_\infty} = \frac{\omega_{LO}^2}{\omega_{TO}^2} \ , \quad (5)$$

where ε_0 is the static permittivity, which includes the lattice contribution, ε_∞ is the electronic contribution,

and ω_{LO} and ω_{TO} are the zone-center longitudinal and transverse optical (LO and TO) phonon frequencies, respectively. The ε_0 of a material is primarily influenced by the lowest-energy TO phonon mode. Although Eu_2TiO_4 is a multi-mode system, Eq. (5) is used here for a qualitative discussion based on a simplified single-mode approximation. Our first-principles calculations on Eu_2TiO_4 (see Table. S4 in SM [51]) identify this as the E_u(TO1) mode, which involves Ti^{4+} and Eu^{2+} ions vibrating against the O^{2-} octahedra within the *a*-*b* plane (see the inset of Fig. 2), analogous to the behavior observed in n = 1 RP-type Sr_2TiO_4 [50]. This finding suggests that the E_u(TO1) mode plays a crucial role in the dielectric properties of Eu_2TiO_4. Specifically, the application of an external magnetic field near T_C can align the Eu spins in the field direction, which may soften the E_u(TO1) mode and increase permittivity. Note that the in-plane movement of the E_u(TO1) mode in the Pv layers of Eu_2TiO_4 closely resembles the T_{1u} mode in $EuTiO_3$ [24], where changes in Eu spin configuration under a magnetic field alter the phonon frequency through modified hybridization between the Eu 4f and Ti 3d orbitals [25]. More detailed analyses of the phonon modes in Eu_2TiO_4 using infrared and Raman spectroscopy [56] should be performed in future work to reveal its phonon nature.

To estimate the Eu/Ti orbital hybridization in Eu_2TiO_4, we calculated the electronic state by site-projected partial density of states (PDOS). The valence band mainly consists of O 2p states, while the conduction band chiefly has Ti 3d and Eu 5d characters. The occupied Eu 4f bands lying between these bands are narrow, indicating their localized nature [see Fig. 4(a)]. The enlarged view of the PDOS in the energy region near the Eu 4f band is shown in Figs. 4(b) and 4(c) for Eu_2TiO_4 and $EuTiO_3$, respectively. The Eu 4f states, which possess the localized spins near the Fermi level, are hybridized with the Ti 3d and O 2p states [see Fig. 4(b)]. Compared to $EuTiO_3$ [Fig. 4(c)], the PDOS for Ti in Eu_2TiO_4 is significantly larger, indicating a stronger hybridization between Eu 4f and Ti 3d orbitals.

To further illustrate the covalent bonding interactions between Eu 4f and Ti 3d orbitals, we employed the COHP method [32]. In COHP analysis, the negative value represents bonding interactions, while the positive value corresponds to antibonding interactions. A comparison of the −COHP in the energy range −1 eV to 1 eV near the Fermi level between Eu_2TiO_4 and $EuTiO_3$ is displayed in Fig. 4(d). Integrating the –COHP curves up to the Fermi level provides the integral –COHP (−ICOHP) value, which qualitatively correlate with the strength of corresponding bonds. The larger positive value of −ICOHP in Eu_2TiO_4 (0.2 $band^{-1}$) than in $EuTiO_3$ (0.17 $band^{-1}$) indicates the stronger bonding between Eu and Ti atoms in Eu_2TiO_4, implying the enhanced AFM interaction within the Pv layers. We expect that this stronger bonding interaction can contribute to the large MD coupling observed in Eu_2TiO_4. Moreover, Figure 4(e) plots the variation in −ICOHP against the isotropic lattice volume change (ΔV). For both Eu_2TiO_4 and $EuTiO_3$, the −ICOHP increases with lattice volume decreasing. Interestingly, the variation in −ICOHP with ΔV is pronounced in Eu_2TiO_4 compared to $EuTiO_3$, which indicates that the layered structure of Eu_2TiO_4 offers a more volume-sensitive mechanism for tuning the bonding interaction between Eu 4f and Ti 3d orbitals. Namely, the pseudo-uniaxial strain resulting from the intrinsic physical nature of the layered perovskite structure provides a versatile platform to study the complex interplay between static electrical and magnetic properties. It is interesting to explore the possibility of inducing ferroelectricity in Eu_2TiO_4 by epitaxial strain or chemical substitution, though care must be taken to mitigate potential conductivity issues.

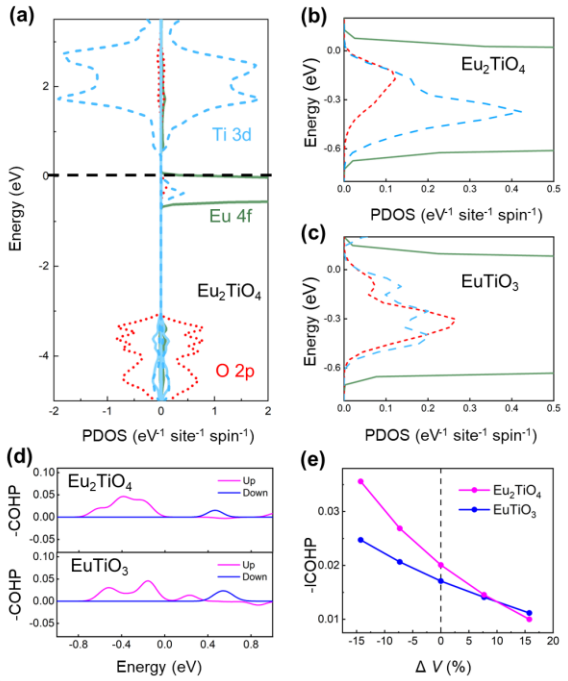

FIG. 4. (a) Site-projected PDOS of Eu_2TiO_4. The zero of energy is placed at the highest occupied state. (b) and (c) Magnified view of the up-spin component of the PDOS in the energy region near the Eu 4f band in (b) Eu_2TiO_4 and (c) $EuTiO_3$. (d) Comparison of −COHP between Eu_2TiO_4 and $EuTiO_3$ without volume change (ΔV = 0%) and (e) variations of integral −COHP (−ICOHP) between Eu_2TiO_4 and $EuTiO_3$ with isotropic volume change (ΔV = −14.3%, −7.3%, 0%,

+7.7% and +15.8%).

V. CONCLUSIONS

In conclusion, an FM layered perovskite oxide, n = 1 RP-type Eu_2TiO_4, exhibits a large MD coupling around T_C. The magnitude of the MD coupling (approximately 22% at 3T) is three times larger than that of bulk $EuTiO_3$. A combined study of structure analysis and first-principles calculations suggests that the enhanced MD coupling in Eu_2TiO_4 arises from the interplay of RS and Pv layers in the quasi-2D structures. The AFM superexchange interactions via the B-site Ti 3d state, which compete with indirect FM interactions via the Eu 5d state, are crucial to the mechanism responsible for the enhanced MD coupling. Our study highlights that this layered structure provides a distinctive approach to regulating MD coupling, opening interesting possibilities for innovative MD material design.

ACKNOWLEDGMENTS

The authors would like to thank Prof. K. Tanaka and Mr. T. Wakamatsu for supporting the electron-beam evaporation. The computation was carried out using the computer resources offered under the category of General Projects by the Research Institute for Information Technology, Kyushu University. This work was supported by the Grant-in-Aid for the Japan Society for the Promotion of Science (JSPS) KAKENHI (Grant No. JP22K04686, JP21H04619, JP23K23043, JP25K08265 JP24K21688, and JP25K01500). K.F. acknowledges grants from the Okura Kazuchika Memorial Foundation, Izumi Science and Technology Foundation, Sumitomo Electric Industries, JFE 21 Century Foundation, and Iwatani Naoji Foundation. SXRD experiments were performed on BL02B2 at SPring-8 with the approval of Japan Synchrotron Radiation Research Institute (JASRI) (Proposal Nos. 2023A1498, 2023B1654, 2024A1510).

[1] H. Schmid, Multi-ferroic magnetoelectrics, Ferroelectrics **162**, 317 (1994).

[2] S. W. Cheong and M. Mostovoy, Multiferroics: a magnetic twist for ferroelectricity, Nat. Mater. **6**, 1 (2007).

[3] K. Dunnett, J.-X. Zhu, N. A. Spaldin, V. Juričić, and A. V. Balatsky, Dynamic Multiferroicity of a Ferroelectric Quantum Critical Point, Phys. Rev. Lett. **122**, 057208 (2019).

[4] N. A. Spaldin and R. Ramesh, Advances in magnetoelectric multiferroics, Nat. Mater. **18**, 3 (2019).

[5] G. Lawes, A. P. Ramirez, C. M. Varma, and M. A. Subramanian, Magnetodielectric Effects from Spin Fluctuations in Isostructural Ferromagnetic and Antiferromagnetic Systems, Phys. Rev. Lett. **91**, 257208 (2003).

[6] P. J. Brown and T. Chatterji, Weak ferromagnetism and magnetic phase transitions in Gd_2CuO_4, Phys. Rev. B **84**, 054426 (2011).

[7] B. B. Van Aken, T. T. M. Palstra, A. Filippetti, and N. A. Spaldin, The origin of ferroelectricity in magnetoelectric $YMnO_3$, Nat. Mater. **3**, 3 (2004).

[8] T. Katsufuji and H. Takagi, Coupling between magnetism and dielectric properties in quantum paraelectric $EuTiO_3$, Phys. Rev. B **64**, 054415 (2001).

[9] C. Jin *et al*., Super-Flexible Freestanding $BiMnO_3$ Membranes with Stable Ferroelectricity and Ferromagnetism, Adv. Sci. **8**, 2102178 (2021).

[10] D. C. Kakarla *et al*., Metamagnetic transitions and magnetoelectric coupling in acentric and nonpolar Pb_2MnO_4, Phys. Rev. B **99**, 195129 (2019).

[11] H. Akamatsu, K. Fujita, H. Hayashi, T. Kawamoto, Y. Kumagai, Y. Zong, K. Iwata, F. Oba, I. Tanaka, and K. Tanaka, Crystal and Electronic Structure and Magnetic Properties of Divalent Europium Perovskite Oxides EuMO$_3$ (M = Ti, Zr, and Hf): Experimental and First-Principles Approaches, Inorg. Chem. **51**, 4560 (2012).

[12] H. Akamatsu, Y. Kumagai, F. Oba, K. Fujita, K. Tanaka, and I. Tanaka, Strong Spin-Lattice Coupling Through Oxygen Octahedral Rotation in Divalent Europium Perovskites, Adv. Funct. Mater. **23**, 1864 (2013).

[13] Y. Hong, P. Byeon, J. Bak, Y. Heo, H.-S. Kim, H. B. Bae, and S.-Y. Chung, Local-electrostatics-induced oxygen octahedral distortion in perovskite oxides and insight into the structure of Ruddlesden–Popper phases, Nat. Commun. **12**, 5527 (2021).

[14] T. Kolodiazhnyi, K. Fujita, L. Wang, Y. Zong, K. Tanaka, Y. Sakka, and E. Takayama-Muromachi, Magnetodielectric effect in $EuZrO_3$, Appl. Phys. Lett. **96**, 252901 (2010).

[15] C.-L. Chien, S. DeBenedetti, and F. D. S. Barros, Magnetic properties of $EuTiO_3$, Eu_2TiO_4, and $Eu_3Ti_2O_7$, Phys. Rev. B **10**, 3913 (1974).

[16] T. R. McGuire, M. W. Shafer, R. J. Joenk, H. A. Alperin, and S. J. Pickart, Magnetic Structure of $EuTiO_3$, J. Appl. Phys. **37**, 981 (1966).

[17] J. H. Lee *et al*., A strong ferroelectric ferromagnet created by means of spin–lattice coupling, Nature **466**, 954 (2010).

[18] K. Tanaka, K. Fujita, Y. Maruyama, Y. Kususe, H. Murakami, H. Akamatsu, Y. Zong, and S. Murai, Ferromagnetism induced by lattice volume expansion and amorphization in $EuTiO_3$ thin films, J. Mater. Res. **28**, 1031 (2013).

[19] R. Zhao *et al*., Emergent multiferroism with magnetodielectric coupling in $EuTiO_3$ created by a negative pressure control of strong spin-phonon coupling, Nat. Commun. **13**, 2364 (2022).

[20] K. Fujita, N. Wakasugi, S. Murai, Y. Zong, and K. Tanaka, High-quality antiferromagnetic $EuTiO_3$ epitaxial thin films on $SrTiO_3$ prepared by pulsed laser deposition and postannealing, Appl. Phys. Lett. **94**, 062512 (2009).

[21] K. Kugimiya, K. Fujita, K. Tanaka, and K. Hirao, Preparation and magnetic properties of oxygen deficient $EuTiO_{3-\delta}$ thin films, J. Magn. Magn. Mater. **310**, 2268 (2007).

[22] S. Li, S. Konishi, T. Kito, K. Fujita, and K. Tanaka, Crystal structure and magnetic properties of $EuZrO_3$ solid solutions, J. Mater. Chem. C **11**, 8383 (2023).

[23] V. V. Shvartsman, P. Borisov, W. Kleemann, S. Kamba, and T. Katsufuji, Large off-diagonal magnetoelectric coupling in the quantum paraelectric antiferromagnet $EuTiO_3$, Phys. Rev. B **81**, 064426 (2010).

[24] V. Goian, S. Kamba, J. Hlinka, P. Vaněk, A. A. Belik, T. Kolodiazhnyi, and J. Petzelt, Polar phonon mixing in magnetoelectric $EuTiO_3$, Eur. Phys. J. B **71**, 429 (2009).

[25] T. Birol and C. J. Fennie, Origin of giant spin-lattice coupling and the suppression of ferroelectricity in $EuTiO_3$ from first principles, Phys. Rev. B **88**, 094103 (2013).

[26] B. J. Kennedy, G. Murphy, E. Reynolds, M. Avdeev, H. E. R. Brand, and T. Kolodiazhnyi, Studies of the antiferrodistortive transition in $EuTiO_3$, J. Phys. Condens. Matter **26**, 495901 (2014).

[27] H. M. Rietveld, A profile refinement method for nuclear and magnetic structures, J. Appl. Crystallogr. **2**, 65 (1969).

[28] V. Petříček, M. Dušek, and L. Palatinus, Crystallographic Computing System JANA2006: General features, Z. Für Krist. - Cryst. Mater. **229**, 345 (2014).

[29] P. E. Blöchl, Projector augmented-wave method, Phys. Rev. B **50**, 17953 (1994).

[30] G. Kresse and J. Furthmüller, Efficient iterative schemes for *ab initio* total-energy calculations using a plane-wave basis set, Phys. Rev. B **54**, 11169 (1996).

[31] G. Kresse and J. Furthmüller, Efficiency of ab-initio total energy calculations for metals and semiconductors using a plane-wave basis set, Comput. Mater. Sci. **6**, 15 (1996).

[32] G. Kresse and J. Hafner, *Ab* initio molecular dynamics for open-shell transition metals, Phys. Rev. B **48**, 13115 (1993).

[33] G. Kresse and J. Hafner, *Ab initio* molecular dynamics for liquid metals, Phys. Rev. B **47**, 558 (1993).

[34] G. Kresse and J. Hafner, *Ab initio* molecular dynamics for open-shell transition metals, Phys. Rev. B **48**, 13115 (1993).

[35] J. Paier, M. Marsman, K. Hummer, G. Kresse, I. C. Gerber, and J. G. Ángyán, Erratum: "Screened hybrid density functionals applied to solids", J. Chem. Phys. **125**, 249901 (2006).

[36] J. Paier, M. Marsman, K. Hummer, G. Kresse, I. C. Gerber, and J. G. Ángyán, Screened hybrid density functionals applied to solids, J. Chem. Phys. **124**, 154709 (2006).

[37] J. P. Perdew, A. Ruzsinszky, G. I. Csonka, O. A. Vydrov, G. E. Scuseria, L. A. Constantin, X. Zhou, and K. Burke, Restoring the Density-Gradient Expansion for Exchange in Solids and Surfaces, Phys. Rev. Lett. **100**, 136406 (2008).

[38] J. P. Perdew, K. Burke, and M. Ernzerhof, Generalized Gradient Approximation Made Simple, Phys. Rev. Lett. **77**, 3865 (1996).

[39] J. P. Perdew, K. Burke, and M. Ernzerhof, Generalized Gradient Approximation Made Simple, Phys. Rev. Lett. **78**, 1396 (1997).

[40] J. Heyd, G. E. Scuseria, and M. Ernzerhof, Erratum: "Hybrid functionals based on a screened Coulomb potential", J. Chem. Phys. **124**, 219906 (2006).

[41] J. Heyd, G. E. Scuseria, and M. Ernzerhof, Hybrid functionals based on a screened Coulomb potential, J. Chem. Phys. **118**, 8207 (2003).

[42] A. V. Krukau, O. A. Vydrov, A. F. Izmaylov, and G. E. Scuseria, Influence of the exchange screening parameter on the performance of screened hybrid functionals, J. Chem. Phys. **125**, 224106 (2006).

[43] A. Togo and I. Tanaka, First principles phonon calculations in materials science, Scr. Mater. **108**, 1 (2015).

[44] R. Nelson, C. Ertural, J. George, V. L. Deringer, G. Hautier, and R. Dronskowski, LOBSTER: Local orbital projections, atomic charges, and chemical-bonding analysis from PROJECTOR-AUGMENTED-WAVE-BASED density-functional theory, J. Comput. Chem. **41**, 1931 (2020).

[45] R. Dronskowski and P. E. Bloechl, Crystal orbital Hamilton populations (COHP): energy-resolved visualization of chemical bonding in solids based on density-functional calculations, J. Phys. Chem. **97**, 8617 (1993).

[46] K. Momma and F. Izumi, *VESTA*: a three-dimensional visualization system for electronic and structural analysis, J. Appl. Crystallogr. **41**, 653 (2008).

[47] J. E. Greedan and G. J. McCarthy, Crystal chemistry and magnetic properties of Eu_2TiO_4 and $Eu_3Ti_2O_7$, Materials Research Bulletin **7**, 531 (1972).

[48] H. Akamatsu, Y. Kumagai, F. Oba, K. Fujita, H. Murakami, K. Tanaka, and I. Tanaka, Antiferromagnetic superexchange via 3d states of titanium in $EuTiO_3$ as seen from hybrid Hartree-Fock density functional calculations, Phys. Rev. B **83**, 214421 (2011).

[49] P. J. Ryan *et al*., Reversible control of magnetic interactions by electric field in a single-phase material, Nat. Commun. **4**, 1334 (2013).

[50] C. J. Fennie and K. M. Rabe, Structural and dielectric properties of Sr_2TiO_4 from first principles, Phys. Rev. B **68**, 184111 (2003).

[51] See Supplemental Material for details about Mössbauer spectroscopy, molecular-field approximation, and first-principles calculations including references [52, 53].

[52] Makoto Wakeshima, Yoshihiro Doi, and Yukio Hinatsu, Mossbauer Effects and Magnetic Properties of Mixed Valent Europium Sulfide, $EuPd_3S_4$. J. Solid State Chem. **157**, 117 (2001).

[53] Chia-Ling Chen and F. De S. Barros, HYPERFINE INTERACTION OF ^{151}Eu IN Eu_2TiO_4. Phys. Lett. A **38**, 427 (1972).

[54] P. Reuvekamp, Kevin Caslin, Zurab Guguchia, Hugo Keller, Reinhard K Kremer, Arndt Simon, Jürgen Köhler and Annette Bussmann-Holder, Tiny cause with huge impact: polar instability through strong magneto-electric-elastic coupling in bulk $EuTiO_3$. J. Phys.: Condens. Matter **27**, 262201 (2015).

[55] T. Kimura, T. Goto, H. Shintani, K. Ishizaka, T. Arima, and Y. Tokura. Magnetic control of ferroelectric polarization. Nature **426**, 55-58 (2003)

[56] R. M. Dubrovin, N. V. Siverin, M. A. Prosnikov, V. A. Chernyshev, N. N. Novikova, P. C. M. Christianen, A. M. Balbashov, and R. V. Pisarev, Lattice dynamics and spontaneous magnetodielectric effect in ilmenite $CoTiO_3$, Journal of Alloys and Compounds **858**, 157633 (2021).